

Automated Grid Refinement Using Feature Detection

Sean J. Kamkar*

Antony Jameson†

Stanford University, Palo Alto, CA 94035

Andrew M. Wissink‡

Ames Research Center, Moffett Field, CA 94035

We investigate feature detection schemes used to guide appropriate mesh resolution for CFD calculations with adaptive mesh refinement (AMR). Methods based on eigenvalues of the velocity gradient, difference between vorticity and strain rate magnitudes, and eigenvalues of the vorticity vector are investigated and compared to traditional vorticity-based detection schemes such as the Q -criterion. We are particularly interested in non-dimensional schemes that do not require the user to dial-in particular values of a quantity to refine to. Results are shown for a variety of analytic and practical test cases.

I. Introduction

IT is well known that the accuracy of computational fluid dynamics (CFD) simulations can be significantly improved by increasing the number of grid points. However, it is impractical to uniformly reduce the mesh spacing throughout the entire computational domain since a large proportion of grid points would be wasted in regions that are not relevant to enhancing the accuracy. Adaptive mesh refinement (AMR) schemes provide a means of placing points only in those regions where they are necessary and can thereby enhance accuracy in an efficient manner. With the dramatic increases in available computational resources, along with the concomitant demands for improved accuracy, AMR schemes are likely to become increasingly important. The schemes developed here are intended for rotorcraft aeromechanics calculations, which have the inherent need to accurately represent vortices in the far-wake.

Rotorcraft flowfields present some unique challenges to computational aerodynamics. Primary among these is the need to accurately capture and preserve the trailing tip vortices that are shed from the spinning rotor blades, which can subsequently interact with the blades themselves, the fuselage and/or the tail rotors. A further important aspect of rotorcraft problems is the close coupling between the CFD and the computational structural dynamics (CSD) solutions. In order to accommodate these challenges, the US Army's High Performance Computing Institute for Advanced Rotorcraft Modeling and Simulations (HI-ARMS) is developing a modular CFD/CSD comprehensive analysis package called Helios.^{1,2} The CFD component of Helios is composed of a unstructured solution strategy in the near-body domain, that is coupled through overset meshes with a high-order adaptive cartesian framework in the off-body domain. The feature detection study, that is the subject of the present paper, is motivated by the need to automate the adaptive Cartesian framework in the in the off-body component of the Helios code.

Pioneering work on hierarchical structured Cartesian-grid AMR was performed by Berger and Oliger³ and Berger and Colella.⁴ This approach was extended to structured curvilinear grids by Berger and Jameson.⁵ Error in the solution was used to determine regions for refinement. Their research highlighted the effectiveness of AMR and demonstrated that considerable gains in efficiency and accuracy can be obtained. Recent AMR work has focused on two possible paths for reducing solution error: adjoint-based analysis^{6–8} and feature-based analysis. Although adjoint-based methods have some attractive aspects, they are limited in their ability to handle unsteady problems such as those encountered in rotorcraft dynamics. Moreover, as discussed earlier, rotorcraft flowfields are characterized by the need to resolve the blade tip vortices and are ideally suited to feature-based AMR strategies.

*Graduate Student, Durand Building, Room 267, Department of Aeronautics & Astronautics, skamkar@stanford.edu, AIAA Member

†Professor, Durand Building, Room 381, Department of Aeronautics & Astronautics, jameson@baboon.stanford.edu, AIAA Fellow

‡Senior Research Scientist, Scaled Numerical Physics LLC, MS 215-1, andrew.m.wissink@us.army.mil, AIAA Member

The paper is organized as follows. After offering some background on feature detection methods, Section III describes the mixed grid solution paradigm used in the Helios code. This involves overset communication between an unstructured near-body solver and an adaptive Cartesian off-body solver. Section IV presents the feature detection algorithms that are targeted towards driving the structured Cartesian mesh refinement in the off-body domain. In Section V, we examine the performance of the feature detection schemes for different two- and three-dimensional test cases: isolated theoretical vortices, tip vortices shed from a NACA 0015 wing section, and the wake of a quarter-scale V22 helicopter rotor in hover. Tagging efficiency and computational performance are catalogued to determine the best approach for driving the Cartesian-AMR procedure for practical rotorcraft computations. In the final section, we provide the conclusions of this study and present some directions for future research and development.

II. Background

Before we discuss different vortex-capturing methods, we should note that a universally accepted definition of a vortex does not exist. Intuitively, a vortex is often considered to be a tube whose surface consists of vortex lines.⁹ This definition can be misleading since a vortex tube does not necessarily imply that a vortex exists. A subjective definition that refers to a vortex as a “multitude of material particles rotating around a common center,” has been proposed by Lugt.¹⁰ Others such as Chong¹¹ and Hunt¹² have used a form of velocity tensor to specify the presence of a vortex. Although the debate over an accepted definition is beyond the scope of this paper, the reader should be aware of the inherent difficulty in automatically detecting a physical attribute that is not clearly defined.

The obvious method of detecting a vortex is to use the magnitude of the vorticity. However, as Jeong¹³ *et al.* has demonstrated, using $|\vec{\omega}|$ is insufficient in a shear flow, especially when the local shear rate is similar to or greater than local vorticity magnitudes. This situation commonly occurs in boundary layer problems where, although the maximum values of $|\vec{\omega}|$ occur at the wall, a vortex does not occur along the wall boundary. A further difficulty with using vorticity, as well as with some of the other commonly used techniques discussed below, is the specification of appropriate threshold values as a criterion for vortex identification. Vorticity is particularly problematic in that purely local information cannot be reliably used to define an appropriate normalization of the vorticity magnitude over a wide range of velocity and length scales. Typically, it is necessary to determine the maximum value of the vorticity (presumably at the vortex center) and a fixed fraction of this maximum value can then be used to specify a “threshold” value. The problem lies in the fact that the maximum vorticity may extend beyond any given grid block and may therefore require additional global feature identification methods to distinguish between multiple vortices in the same flowfield. Therefore to reach our goal of automation, we will not expect the user to know precise levels of vorticity *a priori*. We do not explicitly consider the use of vorticity as a viable option in the current work, although we do employ it to compare and contrast other techniques.

The flow visualization community has largely been responsible for developing a handful of methods that identify “swirling” flow regions without directly calculating vorticity. Chong¹¹ *et al.* used the eigenvalues of the velocity gradient tensor, $\nabla \vec{u}$, to show that a complex eigenvalue pair is associated with a region of swirling motion. This is commonly referred to as the Δ method, as a vortex is found when $\Delta > 0$, where Δ is the determinant of the corresponding cubic equation. Another commonly used criterion is the so-called Q -criterion,¹² which, in addition to being the second invariant of the afore-mentioned cubic equation, Q also represents the difference between vorticity magnitude and local shear strain rate. Additionally, Jeong¹³ *et al.* have developed the λ_2 method, which is based upon the eigenvalues of a symmetric matrix system derived from a quasi-pressure expression. Lastly, Horiuti¹⁴ *et al.* have developed a method to identify vortex sheets, rather than vortex tubes, by examining regions wherein the magnitudes of strain rate and vorticity are high and correlated.

The specific methods considered in this paper include the Δ method, the Q -criterion, the λ_2 method and the $S\text{-}\Omega$ method, along with proposed non-dimensionalized forms of these schemes. These four algorithms, which are described more fully in Section IV, are used as the basis for evaluation and development in the present paper.

One of the problems with applying feature detection techniques in dimensional form is that they require tuning based on the length and velocity scales of the problem. Such tuning parameters are typically problem-dependent, which in turn hinders the automation of the AMR procedure. The main objectives of the present study are therefore to assess different feature-detection techniques and to cast them within an appropriate

non-dimensional context so that a particular scheme and an appropriate non-dimensional threshold can be readily applied to different problems, thereby facilitating a greater degree of automation. We apply the methods to a hierarchy of test cases ranging from simple theoretical vortex cases to more complicated wing and rotor flowfields. By comparing performance for the various cases, we can estimate the accuracy of the vortex tagging as well as the relative efficiency of the different techniques. Furthermore, these methods are compared against more traditional methods like vorticity magnitude and the Q -criterion in order to highlight their degree of general applicability.

III. Flow Solution Paradigm

The Helios code utilizes a dual-mesh overset approach with unstructured mixed-element grids near the body surface and structured Cartesian grids away from the surface. Separate solvers for the unstructured and adaptive Cartesian domains are interfaced through a high-level Python-based infrastructure and domain connectivity software.¹ The rationale of this mixed near/off-body meshing scheme is to apply unstructured grids near the surface to resolve complex geometry and boundary layer effects, and adaptive structured Cartesian grids away from the wall to accurately resolve the far-field wake using time-dependent adaptive refinement¹ (Figure 1).

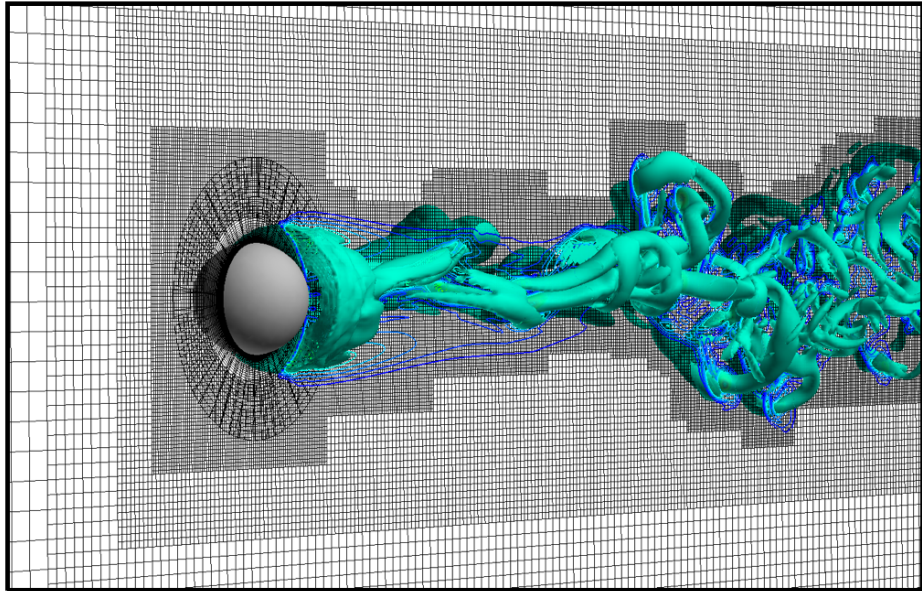


Figure 1: Calculation of $Re=1000$ flow over a sphere using near/off-body gridding approach. The unstructured near-body grid extends a short distance from the surface to capture the viscous boundary layer, adaptive Cartesian grids with a high-order solver are used everywhere else. Shown is an isosurface of vorticity overlaid on the adaptive grid system.

The feature detection schemes investigated in this work are intended to be applied to the off-body Cartesian flow solver, so we focus the remainder of the discussion on this approach. The 3D Euler equations are solved in the off-body region:

$$\frac{\partial \vec{w}}{\partial t} + \frac{\partial \vec{f}}{\partial x} + \frac{\partial \vec{g}}{\partial y} + \frac{\partial \vec{h}}{\partial z} = 0 \quad (1)$$

where the state and flux are

$$\vec{w} = \begin{pmatrix} \rho \\ \rho u \\ \rho v \\ \rho w \\ \rho E \end{pmatrix}, \quad \vec{f} = \begin{pmatrix} \rho u \\ \rho u^2 + p \\ \rho uv \\ \rho uw \\ \rho uH \end{pmatrix}, \quad \vec{g} = \begin{pmatrix} \rho v \\ \rho uv \\ \rho v^2 + p \\ \rho vw \\ \rho vH \end{pmatrix}, \quad \vec{h} = \begin{pmatrix} \rho w \\ \rho uw \\ \rho vw \\ \rho w^2 + p \\ \rho wH \end{pmatrix},$$

where ρ is density, p is pressure, E is the total energy, H is the stagnation enthalpy, and u , v , and w represent the x , y , and z velocities. The governing equations are solved with a 6th-order accurate finite difference scheme as developed by Pulliam,¹⁵ which is specifically optimized for structured Cartesian grids.

The Cartesian grid system is stored as a Berger and Colella⁴-style multi-level block-structured AMR (SAMR) grid hierarchy. Grid levels are constructed from coarsest to finest. The coarsest level defines the physical extent of the computational domain and each finer level is formed by selecting cells on the coarser level and then clustering the marked cells together to form block regions that will constitute the new finer level. The result is a hierarchy of nested refinement levels with each level composed of a union of logically-rectangular grid regions. Construction and storage of this grid system is facilitated by the SAMRAI^{16–18} package from Lawrence Livermore National Lab.

Currently, refinement of the off-body grid system is performed by first marking cells that have vorticity greater than a specified threshold value, and then building new levels from those marked regions. We are primarily interested in time-dependent problems where the grids dynamically adapt, that is they can refine and/or coarsen, to changing features in the flowfield. On a parallel computer system, each “adapt” step requires the grid be repartitioned for load balancing and data communication patterns have to be re-established between processors. The SAMRAI package manages the level construction and all parallel operations in our implementation.

The use of vorticity to mark cells for refinement is a source of difficulty for automation of the AMR process. The local vorticity values would need to be non-dimensionalized by the maximum magnitude within a given vortex. This maximum value may, in fact, occur in a different Cartesian block, which complicates the application of this procedure. Moreover, in complex flowfields, wherein multiple vortices may exist in close proximity, it may further be necessary to distinguish between these different flow features. To address these problems and develop a truly automated AMR procedure, we evaluate alternate feature-detection techniques in this paper, which are described in the following section.

IV. Feature Detection Methods

Four feature detection methods are presented in this section, based on the so-called Q -criterion,¹² the λ_2 criterion,¹³ the eigenvalues of the velocity gradient tensor $\nabla \vec{u}$,¹¹ and the correlation between the symmetric and antisymmetric parts of $\nabla \vec{u}$.¹⁴ For each method, we present some theoretical background and define a threshold function, $f_{threshold}$, which is used for purposes of vortex detection. In each cell, this function is evaluated and the cell is tagged for refinement if the resulting functional value is greater than a pre-specified value of the threshold.

IV.A. Non-dimensional Q

To identify vortical motion, we begin by considering Ω , which represents local flow rotation and is defined as the anti-symmetric part of the velocity gradient tensor, $\nabla \vec{u}$. To obtain a measure of the tensor strength, we apply the Frobenius norm, which for a real matrix is

$$\|M\| = [\text{trace}(MM^T)]^{\frac{1}{2}}.$$

This definition elucidates the significance of $\|\Omega\|$, since $2\|\Omega\|^2 = |\vec{\omega}|^2$, where $\vec{\omega}$ is the vorticity. Apart from considering Ω , we can also use S , which is the symmetric part of $\nabla \vec{u}$ and is a measure of the local strain rate. Using both parameters we can obtain a measure of the *relative* vortical strength. Hunt¹² was one of the first to assess the importance of this relationship, which is often referred to as Q and is usually defined as:

$$Q = \frac{1}{2} (\|\Omega\|^2 - \|S\|^2). \quad (2)$$

In addition to measuring the difference between vorticity and strain rate, Q has additional physical meaning. Q acts as a source term in the Poisson equation for pressure $\nabla^2 p = 2\rho Q$, which is derived from the incompressible form of the Navier-Stokes equations neglecting time dependent phenomena, and body and viscous forces.¹³ This term also appears as the second invariant in the characteristic equation for $\nabla \vec{u}$ and is also discussed in Section IV.C.

Although Equation 2 measures the difference between the rotation and strain rate magnitudes, this parameter is entirely dependent upon the characteristic length and velocity scales of the problem. To yield a suitable non-dimensional form, we can divide by $\|S\|^2$ to obtain a threshold function of

$$f_{threshold} = \frac{1}{2} \left(\frac{\|\Omega\|^2}{\|S\|^2} - 1 \right). \quad (3)$$

Irrational flow occurs when $f_{threshold} \rightarrow -\frac{1}{2}$ and solid body rotation happens when $f_{threshold} \rightarrow \infty$. Positive thresholds indicate regions where the vorticity strength is larger than the shear rate strength. A similar non-dimensional form was explored by Truesdell¹⁹ who formulated the non-dimensional parameter $N_k = \frac{\|\Omega\|^2}{\|S\|^2}$, which regardless of flow speeds, determines the “quality” of rotation.

IV.B. Non-dimensional λ_2

A low pressure region can often coincide with a region of vortical motion. In the simplified case with steady inviscid planar flow, a pressure minimum will occur along the axis which defines the swirling motion when the centrifugal force is balanced by the pressure force. Such a force equilibrium is commonly referred to as a cyclostrophic balance. However, it has been shown¹³ that an unsteady strain rate may cause a pressure minimum in unsteady irrational flow, which indicates that a pressure minimum alone is not adequate for describing a region of swirling motion. Despite this fact, Jeong¹³ *et. al.* used this as a starting point for vortex identification. By discarding 1) unsteady straining, which can create a pressure minimum without requiring vortical or swirling motion, and 2) viscous effects, which can eliminate the pressure minimum in a flow with vortical motion, a better definition of a vortex can be obtained. Starting with the incompressible Navier-Stokes Equation without body forces

$$\left(\frac{\partial \vec{u}}{\partial t} + \vec{u} \cdot \nabla \vec{u} \right) = \frac{1}{\rho} (-\nabla p + \mu \nabla^2 \vec{u}), \quad (4)$$

where \vec{u} is velocity and μ is viscosity. We can take the gradient of the entire equation, which will allow us to refer to the term on the left hand side as the acceleration gradient $a_{i,j}$. This acceleration gradient can be decomposed into the same symmetric (S) and antisymmetric (Ω) parts and as before. After some algebra and applying the previous assumptions

$$-\frac{1}{\rho} p_{,ij} = \Omega_{ik}\Omega_{kj} + S_{ik}S_{kj}. \quad (5)$$

The eigenvalues of $S^2 + \Omega^2$ are used to define vortical motion:

$$[S^2 + \Omega^2 - \lambda_i I]X_i = 0, \quad (6)$$

where I is the identity matrix and λ_i and X_i represent the i^{th} eigenvalue and its corresponding eigenvector. A negative eigenvalue indicates that a “pressure minimum” occurred in a plane defined by the corresponding eigenvector. Since a vortex core is not defined by a plane, but by an axis, we will look for the presence of two negative eigenvalues. In other words, if we order the eigenvalues such that $\lambda_1 \leq \lambda_2 \leq \lambda_3$, the condition $\lambda_2 < 0$ indicates the presence of a vortex.

Since it is advisable to non-dimensionalize λ_2 so that it remains well scaled for a variety of flow cases, similar to Section IV.A, we will use $\|S\|^2$ to define a threshold function

$$f_{threshold} = -\frac{\lambda_2}{\|S\|^2}. \quad (7)$$

The negative sign has been inserted so that a positive threshold value may be used to control refinement. Although it is a little less intuitive in this case, λ_2 and $\|S\|^2$ have similar scalings (and units) since both represent velocity gradients. This definition also creates a suitable normalization, since $\|S\|$ will be relatively small in regions of vortical flow and large in regions outside a vortex.

IV.C. Modified Δ

Chong¹¹ *et. al.* investigated how three dimensional flow fields may be classified using the eigenvalues of the velocity gradient tensor. By applying techniques of critical point theory, a local Taylor series expansion of the flow can be used to describe topological features of flow patterns. Similar to the eigenvalue problem of Equation 6, the eigenvalues of $\nabla \vec{u}$ reveal information about the local flow field and the solution to the corresponding problem for a 3D case is

$$\lambda^3 + P\lambda^2 + Q\lambda + R = 0, \quad (8)$$

where $P = -\text{trace}[\nabla \vec{u}]$ (and equals zero for an incompressible flow), $Q = (P^2 - \text{trace}[(\nabla \vec{u})^2])/2$, and $R = -\det[\nabla \vec{u}]$. The solution to Equation 8 will either yield three real roots ($\lambda_{r1}, \lambda_{r2}, \lambda_{r3}$) or a single real root with a complex pair ($\lambda_r, \lambda_{cr} \pm \lambda_{ci}$). If the latter case occurs, local swirling motion exists. Moreover, the eigenvalues also contain additional information and Figure 2 shows how λ_r , λ_{cr} , and λ_{ci} can affect local kinematics. The sign and magnitude of a real eigenvalue λ_r determine the acceleration and direction of the

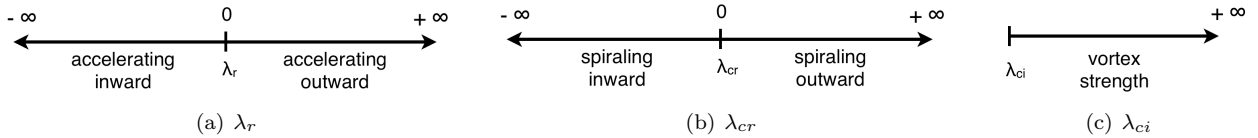


Figure 2: A demonstration of how eigenvalues of $\nabla \vec{u}$ effect particle motion.

particle along a path determined by its corresponding eigenvector. The real part of the complex pair λ_{cr} indicates whether or not the flow is swirling into or out of its center and λ_{ci} indicates the swirling (vortical) strength.

Since λ_{ci} is a measure of rotational strength, we expect a high correlation between it and the vorticity. However, to make it practical for our current purpose, this parameter is non-dimensionalized by $\|S\|$, so that the threshold function is defined as:

$$f_{threshold} = \frac{\lambda_{ci}}{\|S\|}. \quad (9)$$

Note that λ_{ci} is non-dimensionalized by $\|S\|$ for consistency, and not by $\|S\|^2$ as was done in the previous cases.

IV.D. Correlation between S and Ω

The turbulence community has long addressed the task of classifying *coherent structures*. These structures are identifiable topologies found in turbulent flows that have similar observable characteristics. These structures may be roughly classified into two groups: those with vortex tube-like structures, and those with vortex sheet-like structures.²⁰ Although this classification is useful, we should bear in mind that they often coexist, since a vortex tube is initially formed from the roll up of a vortex sheet.

The three previous methods have been designed to pinpoint vortex cores and here, we examine a method that attempts to locate a vortex sheet. To identify regions of vortex sheets, we will leverage the fact that strain and rotation rates are correlated, and that both have large magnitudes in vortex sheets. Horiuti¹⁴ *et al.* suggested the following eigenvalue problem

$$[S\Omega - \Omega S - \lambda_i I]X_i = 0. \quad (10)$$

The term $(S\Omega - \Omega S)$ is also found in the anti-symmetric part of a simplified form of the Reynolds stress tensor.²¹ Since this method looks for large positive eigenvalues contained in a vortex plane, the search is constrained to planes that are normal to the vorticity vector. Therefore, the eigenvalue associated with the eigenvector that is maximally aligned with the vorticity vector is ignored, and λ_+ (the second largest remaining eigenvalue) is used to control mesh refinement. This eigenvalue is also non-dimensionalized by $\|S\|^2$, but an offset is added since we are looking for regions where the vorticity strength is greater than the

shear rate strength (as was the case for the non-dimensional Q method), so we define

$$f_{threshold} = \frac{\lambda_+}{\|S\|^2} - 1. \quad (11)$$

In all of the above cases, the threshold function is used to mark mesh cells for refinement if its value is greater than a pre-specified threshold value. For the non-dimensionalized Q and $S\text{-}\Omega$ correlation methods, functional values greater than zero represent regions where the vorticity is higher than the shear strain rate, whereas positive functional values indicate the presence of vortical flow for the modified Δ and λ_2 methods. Suggested threshold values for each method are given in concert with the testing results in the following section.

V. Results

A suite of theoretical and practical test cases was used to analyze the feature detection schemes in detail. We began with three theoretical cases that were useful for the calibration and validation of the methods: these included an incompressible Lamb vortex, two interacting incompressible Lamb vortices, and a 3D ring vortex. In all cases, we cataloged the performance of the methods in terms of the fraction of the vortex tagged and the computational efficiency. Following this, more realistic cases were considered, such as flow over a NACA 0015 airfoil and a V-22 TRAM rotor in hover, in order to demonstrate the comparative performance of the different methods for practical problems. One of the key objectives of these studies was to derive fully-automated tagging procedures that can be reliably used without special tuning for a wide variety of applications. In particular, we stress the importance of the proposed non-dimensionalized forms of the feature detection methods and the specification of a *constant* threshold value as a tagging criterion in each method.

The methods of Section IV were compared to the results obtained using the traditional vorticity magnitude and/or the dimensional- Q methods. In applying the vorticity method, we chose to tag all cells with a vorticity magnitude greater than 10% of the maximum vorticity. The choice of 10% was arbitrary, but it provided a useful means of comparison, particularly for the theoretical cases. Additionally, average execution run times per cell were tabulated (ratio of total run time to number of grid cells). For the results shown here, the code was compiled with the Intel Fortran Compiler 10.1 using optimization flags on an Intel Core 2 Duo processor operating at 2.4 GHz with 4 GB of RAM. We further note that the implementation of the methods was optimized for Cartesian cells since our primary interest is targeted towards the AMR procedure in the off-body solver of the Helios code.

V.A. Theoretical Test Cases

In this section, we describe the application of the feature detection methods to several classical flowfields, such as the 2D Lamb vortex, co-rotating and counter-rotating Lamb vortices and a 3D ring vortex. Because of the familiarity of these flowfields and the existence of analytical solutions, these test cases are used to carefully vary parametric effects such as Mach number, vortex strength and size, vortex separation distance and grid resolution. In addition, the last test case demonstrates performance in the presence of 3D effects, such as the misalignment of the vortex and the Cartesian grid system.

V.A.1. Incompressible Lamb Vortex

As a first test case we considered the classical 2D Lamb vortex. This test case provided a simple means of comparing against the exact vorticity solution and is therefore useful for verifying the proper non-dimensionalization of the different feature detection techniques considered here. The incompressible Lamb vortex solution is given by:

$$V_\theta = \Gamma \left(\frac{1 - e^{-(\frac{r}{a})^2}}{r} \right), \quad (12)$$

where V_θ is the velocity in the θ direction, Γ is the circulation strength, r is the radial distance from the vortex center, and a is the radial vortex "size". This radial decay parameter approximately corresponds to the distance at which the vorticity magnitude has reduced by an order of magnitude from the maximum

value and was used in our assessments to specify the grid region for which the vortex tagging is considered to be 100%.

Several parameters such as vortex strength, size and grid resolution were varied in our studies. As an example, specific results obtained by varying the grid resolution are considered first. Figures 3(a-c) show the vortex with fine (about 19 points across the vortex), medium (about 11 points) and coarse (about 5 points) resolutions. In each case, the maximum vorticity magnitude is 7.89 1/s.

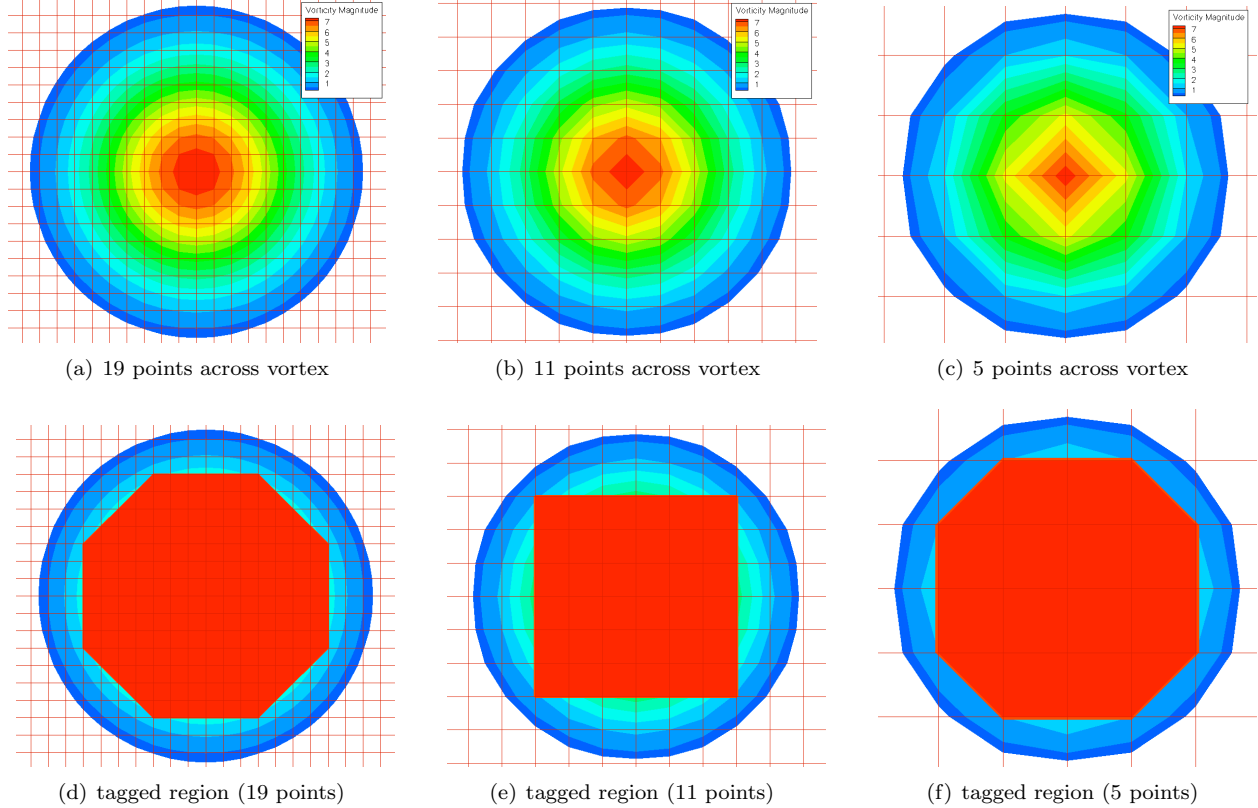


Figure 3: Contour plot of vorticity for single vortex case, clipped below 10%, on different computational meshes (top row). Tagged region found by the modified Δ method (bottom row). Some cells appear to be “half-tagged” which was a result of interpolation by the post-processing visualization software. These half tagged cells were not tagged, but showed up nonetheless due to interpolation between cells.

All the methods were run with a threshold value of zero and the percentage of the vortex tagged by the method (as compared to the ideal tagging based on the theoretical vortex size) is listed in Table 1. It is interesting that, for this simple case, each of the methods performed identically—capturing 50% to 60% of the total vortex. For illustration purposes, Figures 3(d-e) illustrate the cells (shown in red) that were tagged by the modified Δ method. (Corresponding results for the other techniques look similar for this case.) Results for varying vortex strength and size also yield similar results and are not shown for that reason.

Bear in mind that even though the percentage of cells tagged fell between 50% and 60% for each method, this region includes about 75% of the radial extent of the vortex. Moreover, the tagging percentage will be higher or lower based upon the precise definition of the vortex size. The Cartesian mesh refinement procedure in SAMRAI will naturally add buffer cells around the tagged region in order to ensure a smooth transition between the coarse background mesh and the fine adaptive mesh around the vortex. With these considerations, the 50-60% range shown in Table 1 are considered acceptable for a 2D problem.

Execution times for the different techniques are given in Figure 4. In addition to the four proposed methods, vorticity based detection has also been added for comparison purposes. The non-dimensionalized λ_2 and $S\cdot\Omega$ correlation methods were the most computationally expensive since each required a symmetric eigenvalue solution (calculated here using LAPACK routines). The non-dimensional Q method and the modified Δ method, on the other hand, are very economical, running about three times faster than the non-dimensional λ_2 method and about five times faster than the $S\cdot\Omega$ correlation method. Moreover, the run

	Points Across a Vortex		
	5	11	19
Non-dim Q	50	58	55
Non-dim λ_2	50	58	55
Modified Δ	50	58	55
$S\cdot\Omega$ Correlation	50	58	55

Table 1: Percentage of points tagged with a vorticity level higher than 10% for a single vortex. A vortex with 5, 11, or 19 points across the vortex diameter was considered.

times of the non-dimensional Q and modified Δ methods are nominally of the same order as the traditional vorticity method. Although the modified Δ method also requires an eigenvalue solution, it was only needed in regions where the discriminant of Equation 8 was less than zero, which explains its reasonable cost.

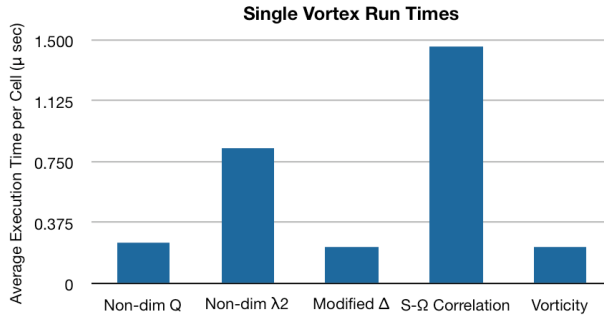


Figure 4: Comparison of feature detection run times for the single vortex case, along with the vorticity magnitude method. Times listed, which were averaged over the 5, 11, and 19 point cases, represent total run time divided by the number of grid cells.

As a final study of the 2D Lamb vortex, we carried out a sensitivity study (Figure 5) that demonstrated how the methods perform as the threshold value was increased. Sensitivity of the results to the threshold value is important when we consider practical test cases, where small flow disturbances and solution noise is present. For such cases, if a threshold value of zero is applied, the grid cells corresponding to these small fluctuations will be likely tagged for refinement, leading to significant “over-tagging”. However, increasing the threshold value will have the effect of tagging a smaller percentage of the vortex as seen in Figure 5. Of the four methods considered, the drop-off in cells tagged was the least for the identically performing non-dimensional Q and λ_2 methods, while the other two methods performed more-or-less comparably. Recall that in Section IV.A we discussed the relationship between Q and the pressure, so this strong correlation was expected. For a threshold value of two, the non-dimensional Q and λ_2 methods tagged about 30% of the cells, which corresponds to about 55% of the radial extent of the vortex. Overall, we note that all the methods still tag the vortex reasonably well even for relatively large threshold values.

V.A.2. Two Incompressible Lamb Vortices

A critical aspect of rotorcraft flowfields is the co-existence of multiple vortices in close proximity to each other. One scenario involves two (or more) co-rotating vortices that have originated from the tips of the different rotor blades. Additionally, counter-rotating vortex pairs are also commonly encountered in aerodynamics. For this reason, we considered both situations. In addition to vortex strength and size, we also varied the vortex separation distance in our parametric studies. In the specific results shown here, we have utilized the finely resolved vortex test case from the previous section, i.e., with a grid resolution of 19 points across the vortex and a vortex strength of 7.89 l/s . Two such identical vortices were then positioned at distances of $2.0 d$, $1.0 d$, and $0.5 d$, where d is the vortex diameter. Both co-rotating and counter-rotating cases are shown in Figures 6(a,b). Note that the centers of “swirling motion” do not reside in regions with highest vorticity magnitude, but all four feature detection methods successfully captured the regions of maximum

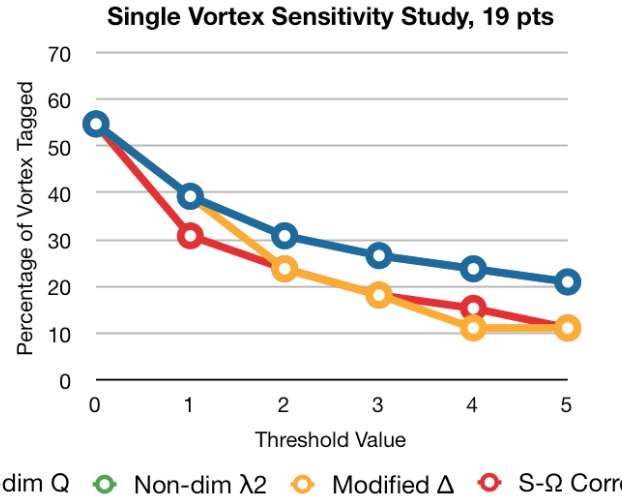


Figure 5: A sensitivity study for the single vortex case with 19 points across the diameter illustrates how decreasing the threshold value for each method reduces the number of points tagged. The performance non-dimensional λ_2 method (green) coincided with the non-dimensional Q method (blue).

vorticity. In the tagging results shown in Figures 6(c,d), the non-dimensional Q method was used with a threshold value of zero. Similar results were obtained with the other methods.

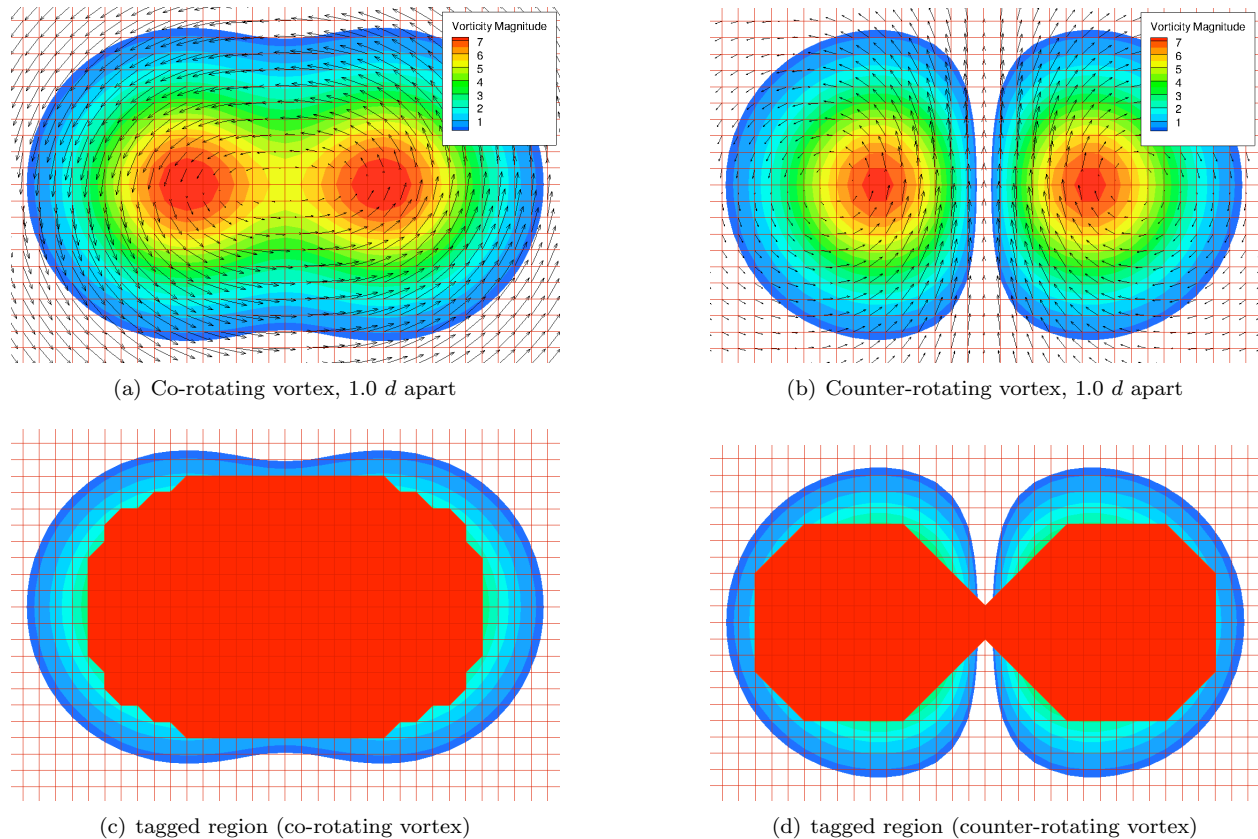


Figure 6: Contour plot of vorticity for multiple vortex case, clipped below 10%, with computational mesh (top row). Tagged region located by the non-dimensionalized Q method (bottom row). Explanation of “half-tagged” is given in caption for Figure 3.

The results of the four methods with a zero threshold value for different separation distances applied

to the co- and counter-rotating cases are given in Table 2. Similar to the single vortex case, each method performed identically, tagging between 50% to 65% percent of the points. Moreover, the effects of separation distance and the relative directions of rotation are limited with the counter-rotating cases registering slightly lower tagging percentages. The run times for the different methods and additional parameter sensitivities are not given because these results are quite similar to the single vortex case. In conclusion, we note that consistently all methods tagged identical grid areas, and the modified Δ and non-dimensionalized Q methods are again preferable due to their shorter run times.

	Separation Distance					
	Co-rotating Vortex			Counter-rotating Vortex		
	0.5 d	1.0 d	2.0 d	0.5 d	1.0 d	2.0 d
Non-dim Q	55	65	56	56	53	52
Non-dim λ_2	55	65	56	56	53	52
Modified Δ	55	65	56	56	53	52
$S\text{-}\Omega$ Correlation	55	65	56	56	53	52

Table 2: Percentage of points tagged with a vorticity level higher than 10% for co- and counter-rotating cases. Separation distances of 0.5, 1.0, and 2.0 radial diameters was evaluated for a vortex with a core radius of 0.5 m.

V.A.3. 3D Ring Vortex

The final theoretical test case is an isolated ring vortex that was studied to verify the performance of the methods in three dimensions and to understand the effects of a non-aligned grid-vortex system. The ring vortex exact solution was originally developed by Z.J. Wang of Iowa State University as a test case for DARPA's Helicopter Quieting Program (HQP) and it calculates initial velocities using a code supplied by HyPerComp, Inc. The vortex used for this case had an outer ring radius of 0.5 m, a core ring radius of 0.25 m, a maximum vorticity magnitude of 19.8 1/s, and a maximum velocity magnitude of 1.15 m/s. A vorticity isosurface and the corresponding velocity field is illustrated in Figure 7a. The region of cells tagged by the non-dimensionalized λ_2 method (looking at an y - z cutting plane) is shown in Figure 7b. Again, the colored region surrounding the tagged cells represents the vortex size based on an isosurface that is 10% of the maximum vorticity magnitude.

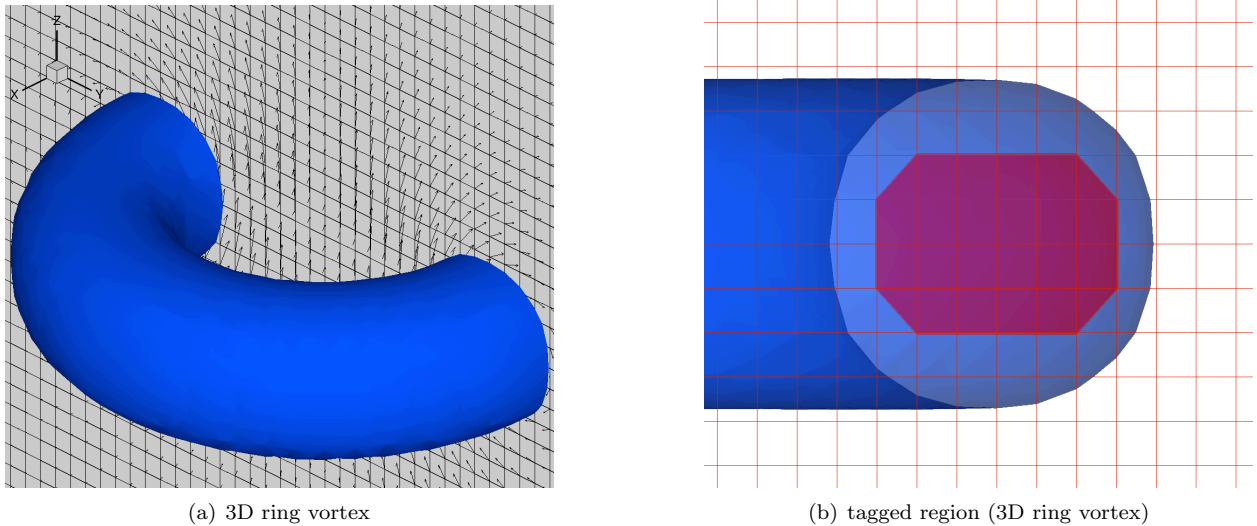


Figure 7: Ring vortex with isosurface at 10% of max vorticity and a y - z cutting plane containing velocity field and computational mesh (left). Plot of y - z plane with isosurface of 10% of max vorticity (blue), computational mesh, and tagged region by the non-dimensionalized λ_2 method (magenta).

Each method tagged about 41% of the vortex when a threshold value of zero was applied and a parameter

study can be found in Figure 8. The lower value of the tagging percentage is attributed to the 3D nature of the flow, but still corresponds to about 65% tagged in terms of the radial size of the vortex. Figure 8 also shows the sensitivity of the results to the variation of the threshold value. Although the percentage of cells tagged shows a steeper initial decrease when the threshold parameter is increased to two, the tagged percentage remains relatively constant for higher threshold values. Categorizing this type of behavior is important for practical problems in which higher threshold values will be used to avoid tagging features that resemble vortices, but in fact represent solution noise and other small scale phenomenon. Indeed, these results show that, by applying high threshold values, the detection algorithms can avoid tagging “quasi-vortex” structures apparent in complex simulations, while still being able to correctly identify the vortex cores.

Finally, we again note that the modified Δ and non-dimensionalized Q methods were preferable because of their relatively quick execution. The execution times are not provided since they are quite similar to the results given earlier.

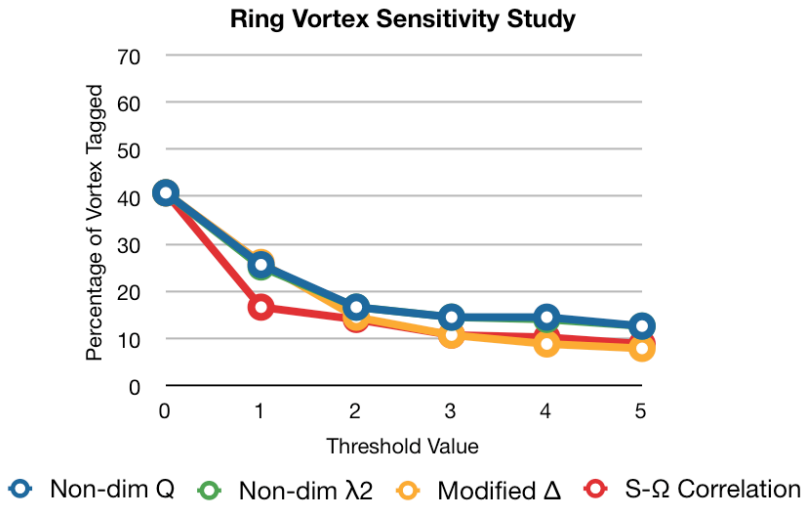


Figure 8: A sensitivity study for the 3D ring vortex case shows the effect of increasing threshold on the percentage of points tagged.

V.B. Practical Test Cases

Having demonstrated the performance of the methods for a variety of theoretical cases, we now consider two practical flow cases: flow over a NACA 0015 square wing and a quarter-scale V-22 (TRAM) rotor in hover. In both cases, we obtained solutions from the Helios code using static refined grids. The feature detection techniques were applied to the corresponding off-body mesh solutions. Cells were marked according to the specified threshold value. We note that these cases are completely general and the feature detection methods are in no way tuned to these particular flowfields. Finding the appropriate threshold value for tagging with traditional methods such as vorticity magnitude or dimensional-Q can be challenging for problems of this type. This underscores the importance of pursuing non-dimensionalized forms of the feature detection techniques that can be used across different problems.

V.B.1. NACA 0015 Wing Flowfield

The first practical test case is the steady flow around a full-span NACA 0015 wing at a Mach number of 0.1235 with 12 degrees angle of attack at a Reynolds number of 1.5×10^6 . The solution was computed by the Helios code with a grid system comprised of structured curvilinear grids in the near-body domain and refined structured Cartesian grids in the off-body domain. The near-body calculations were performed by the UMTURNS code of Sitaraman and Baeder.²² The off-body solutions were computed with the SAMARC module with a 6th-Order central finite difference discretization. The PUNDIT²³ software performed the near-off-body domain connectivity. As noted earlier, the feature detection schemes in this case were applied solely to the Cartesian mesh blocks that comprise the off-body grid system. Mesh cells were tagged according

to the local value of the threshold function and the results are compared with traditional methods. Note that our goal is to determine the optimal feature detection procedures to tag the Cartesian off-body meshes for refinement. The Cartesian grids in this case were refined to regions of high vorticity magnitude, we did not attempt to use the tagged cells from the feature detection algorithms to drive the adaptive solution procedure, although this is of course our long-term objective.

Figure 9 shows the evolution of the vortex structures from the tip of the wing. The flowfield is dominated by the presence of a vortex sheet which rolls up into a strong tip vortex close to the wing. The tip vortices remain coherent up to about 15 chord lengths behind the wing and then begin to break down into smaller structures. Adaptive Cartesian grids with four levels of refinement were used in this solution to refine the mesh to capture the regions of high vorticity. Near the wing in the finest levels of the off-body mesh, the vorticity is seen to be high, about 910 1/s , but further downstream, in the coarse grid system, this value is reduced by two orders of magnitude. This vortex dissipation makes vorticity tagging an unreliable method for resolving the vortex far downstream of the wing.

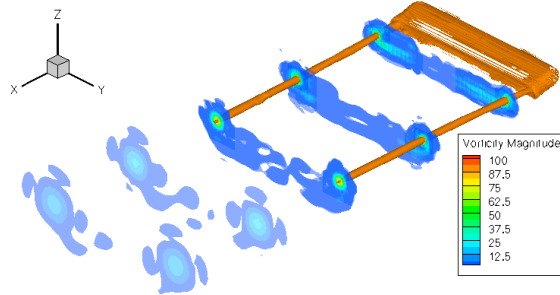


Figure 9: NACA 0015 case with an isosurface (orange) of vorticity magnitude at $t_{val} = 10\%$ maximum vorticity. Five cutting y - z planes with contours of vorticity are shown for illustration.

Figure 10 shows results for the NACA 0015 wing solution with cell-tagging based on a local vorticity magnitude method as well as the dimensional- Q criterion. In each case, results are shown for two different choices of the threshold value (t_{val}). In the case of the vorticity method, the maximum vorticity was computed and all cells are tagged that have a value higher than the percentage of this value defined by t_{val} . Here we notice the dependence upon the grid system used, as the “maximum” value calculated varies in each grid block. This allowed the scheme to identify the trailing tip vortices well into the far field, but also concentrated a heavy region of points in the wake. Similarly, for the dimensional- Q method (Equation 2) all cells with a value higher than t_{val} were tagged and like vorticity, this method also identified a large region of the wake. Not only did these methods struggle to distinguish between the trailing tip vortex cores and the wake, more importantly we see that the tagged region is strongly dependent on the threshold applied.

Figure 11 shows corresponding tagged cell regions using the modified Δ and the non-dimensional Q methods with thresholds of 2.5 and 4.5 respectively. Recall that the sensitivity studies given earlier (Figures 5 and 8) illustrate that a threshold of 2.5 for modified Δ and $S\text{-}\Omega$ methods tagged approximately as many points as the non-dimensionalized Q and λ_2 methods did using a threshold of 4.5. Both methods recognized the trailing tip vortices well into the far field and manage to tag fewer points in the wake region. Unlike in Figure 9, where the identified vortex stops before entering the “coarse-grid” region, these methods use purely local information in calculating the threshold function, which allowed it to identify the trailing tip vortices, even after they were significantly attenuated downstream. The $S\text{-}\Omega$ correlation and the non-dimensional λ_2 methods reveal similar results with respective thresholds of 2.5 and 4.5.

Additionally, the run times (Figure 12) for the different techniques are also given. It is apparent that the $S\text{-}\Omega$ method is the slowest, taking about an order of magnitude longer than the vorticity, the modified Δ and the non-dimensional Q methods. As before, this result is anticipated since the more efficient methods do not require that an eigenvalue solution to be obtained in each grid cell.

V.B.2. V-22 TRAM Rotor

The final test case is the quarter-scale V-22 (TRAM) rotor in $\text{Mach} = 0.1$ climb conditions (Figure 13). Performance prediction of the rotor generally requires precise resolution of the wake vortices. As in the last case, a previously obtained Helios solution was used as the basis for these studies. A total of five levels

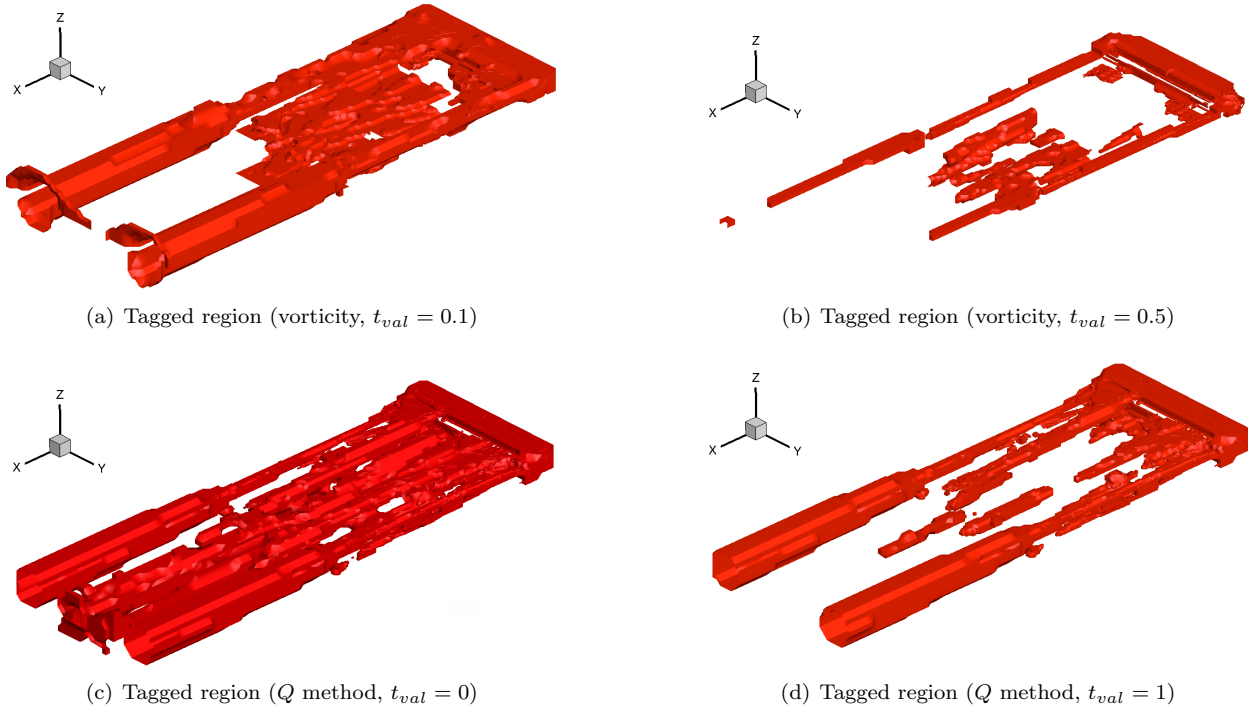


Figure 10: Identified regions for the NACA 0015 case by the vorticity (top) and dimensional Q methods (bottom). Both methods marked cells in the wake region to varying degree with large dependence on the particular threshold value (t_{val}) chosen.

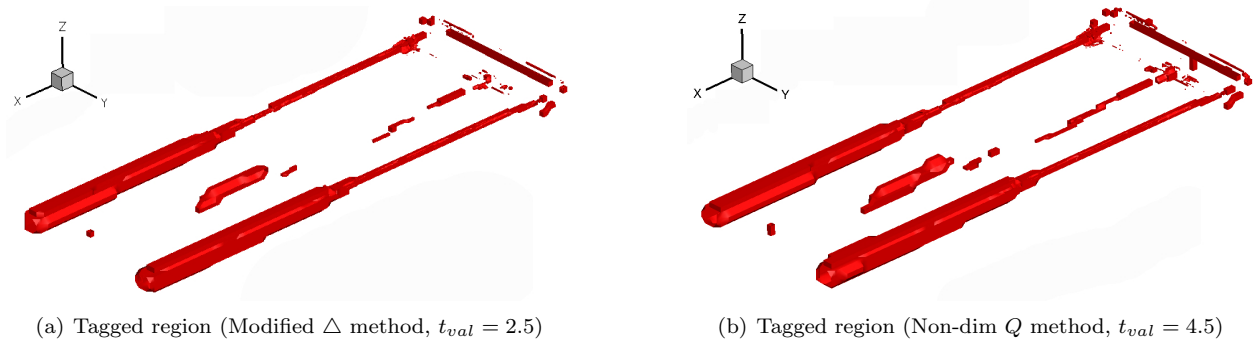


Figure 11: Identified regions for the NACA 0015 case by non-dimensional methods utilizing a fixed threshold value.

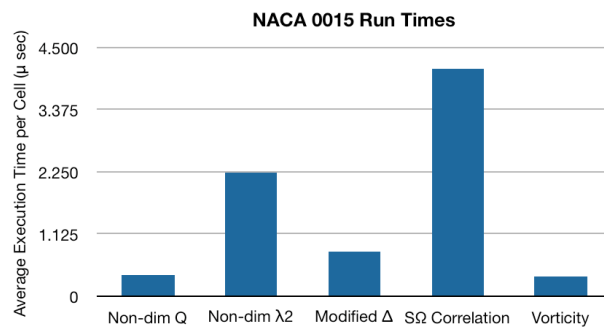


Figure 12: NACA 0015 Case: Run Times

of Cartesian refinement are used in this base off-body solution and the Cartesian flow solver is 5th order accurate in space. The off-body mesh solution was then run through the different feature detection methods and the cells were tagged for evaluation purposes. Again, no attempt was made to use the tagged regions to drive the process of mesh adaptation.

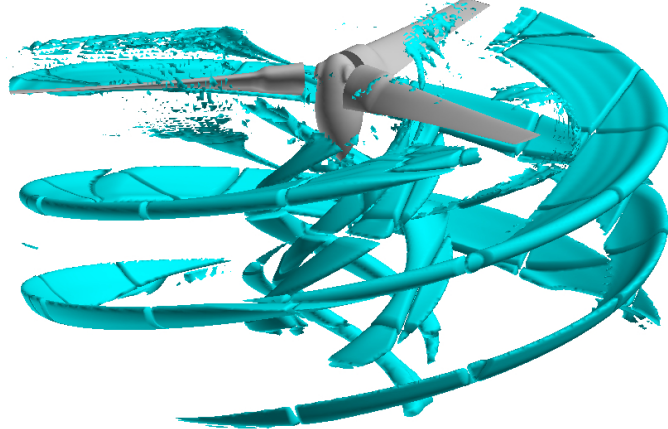


Figure 13: V-22 TRAM case with rotor and an isosurface drawn at 25% of maximum vorticity

As in the NACA 0015 case, to show the difficulty associated with “tuning” the threshold value, we present results for the dimensional Q method (Figure 14). For three threshold values ($t_{val} = 0.005, 0.025, 0.05$), the Q method shows two notable qualities. First, the appropriate values are two orders of magnitude lower than those for the NACA 0015 case, thereby demonstrating the key problem with detection schemes that utilize a dimensional form. Second, even after the appropriate scale has been determined, the process of selecting an appropriate value requires user input. It is certainly possible to further fine-tune these methods, but the optimal threshold values are still going to be problem-dependent, making automation of the refinement procedure difficult.

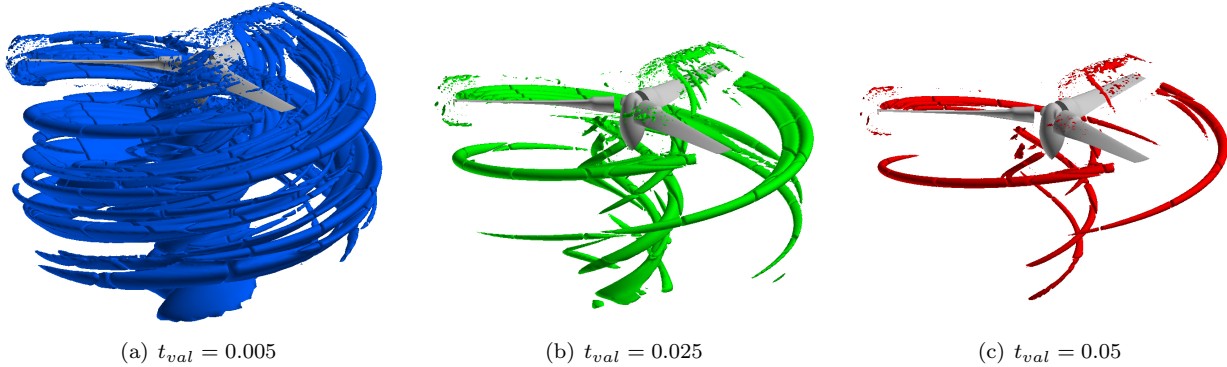


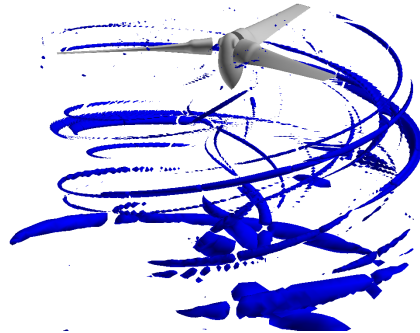
Figure 14: Three figures demonstrating the difficulty in “tuning” to find the proper level of identification for the dimensional Q method (Equation 2) for the V-22 TRAM case. Not only is the optimal t_{val} unknown *a priori*, it may change during an unsteady simulation, further hindering the goal of automation.

As previously stated, we desire feature detection methods that will yield proper vortex tagging using *fixed* threshold values for a wide spectrum of problems and flow regimes. Figure 15 shows the tagged results for the modified Δ and the non-dimensional Q methods. Similar to the NACA 0015 case, the other plots have been omitted because the $S\text{-}\Omega$ method resembled the modified Δ method and the non-dimensional λ_2 method resembled the non-dimensional Q method. In these results, the same threshold values were used as in the NACA 0015 case—i.e., $t_{val} = 2.5$ for the modified Δ and the $S\text{-}\Omega$ methods, and $t_{val} = 4.5$ for the λ_2 and the non-dimensionalized Q methods. A fixed threshold, which works reasonably well for both practical test cases, is not possible with either the vorticity or dimensional Q methods.

The tagged region is shown in greater detail (Figure 16), where a cutting plane illustrates vorticity



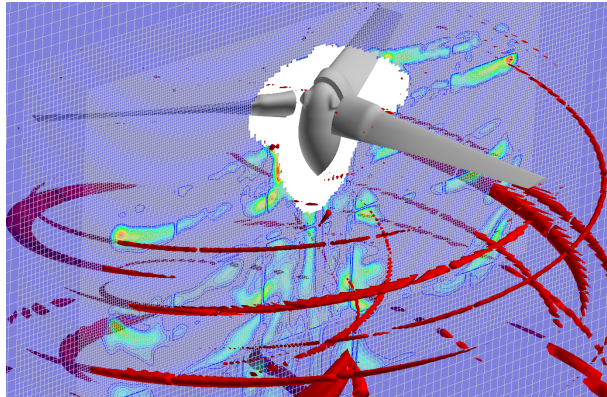
(a) Tagged region (modified Δ , $t_{val} = 2.5$)



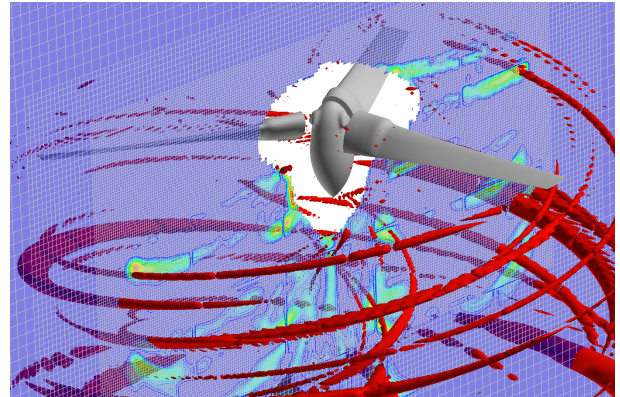
(b) Tagged region (non-dimensional Q , $t_{val} = 4.5$)

Figure 15: The modified Δ and non-dimensional Q methods applied to the V-22 TRAM case. The cutting plane contains the computational mesh of the off body grid along with the vorticity magnitude contours. The red isosurfaces represent the tagged region by the respective method.

contours. Although not exact, the schemes identified the corkscrew-like motion associated with the trailing tip vortices. We notice that the schemes picked up other features did not directly overlap with regions of higher vorticity. Remember that vorticity alone failed to capture all the appropriate regions in the NACA 0015 case (Figure 9) and additional work is required to understand the importance of these regions. In addition to locating the trailing tip vortices, all the methods tagged a relatively small region located directly below the propeller hub.



(a) Tagged region (modified Δ , $t_{val} = 2.5$)



(b) Tagged region (non-dimensional Q , $t_{val} = 4.5$)

Figure 16: The modified Δ and non-dimensional Q methods applied to the V-22 TRAM case. The cutting plane contains the computational mesh of the off body grid along with the vorticity magnitude contours. The red isosurfaces represent the tagged region by the respective method.

We must re-emphasize that these results were not tuned in any way and the relative invariance of the threshold values suggests that these non-dimensionalized forms of the methods can be successfully automated within a computational platform. Indeed, these initial results are encouraging and future work will focus on incorporating one or more of the proposed techniques within the adaptive grid framework of the Helios platform.

VI. Concluding Remarks

We evaluated different vortex detection techniques for feature detection within the AMR adaptive gridding approach used in the Helios software. Four particular schemes were evaluated, the modified Δ , $S\text{-}\Omega$ correlation, non-dimensionalized λ_2 and non-dimensionalized Q methods. We specifically focused on the de-

velopment of non-dimensionalized forms of these methods which can be used across a wide range of problems and flow regimes, in order to avoid the problem dependence associated with refining to particular values of vorticity magnitude or Q . Our ultimate goal is to automate the refinement procedure by removing the need for the end user to specify the flow quantity and value which drives the refinement.

Using a hierarchy of simple theoretical cases and complex practical flowfields, we have successfully demonstrated the ability to detect vortical flow over a range of flow regimes. In all cases, we verified that it is possible to operate these methods without requiring parameter tuning on a case-by-case basis. For practical flowfields, the proposed techniques are superior to the conventional vorticity magnitude and dimensional Q method. Assessments of the CPU run times for each method suggests that computing an eigenvalue solution at each grid cell is relatively expensive and is impractical for related applications. The non-dimensionalized Q method and the modified Δ method, which do not require such eigenvalue computations, perform the best and are typically comparable in execution times to the standard vorticity method. Overall, these two methods – the non-dimensionalized- Q method and the modified Δ method – show the most promise of the methods evaluated for practical applications in terms of tagging accuracy and computational efficiency.

Application of these methods to in a practical setting was limited to two problems in this work. More analysis is necessary to determine whether the conclusions drawn apply more generally. Also, we did not investigate the capability of the refinement triggered by these methods to accurately capture the aerodynamics loads or compare the predicted vortex locations to experimental data. We intend to address these issues in future work.

Acknowledgments

The primary author and Prof. Jameson have been supported by the joint NASA-Stanford fellowship program (Grant #1108061-1-RANJF). Material presented in this paper is a product of the CREATE-AV Element of the Computational Research and Engineering for Acquisition Tools and Environments (CREATE) Program sponsored by the U.S. Department of Defense HPC Modernization Program Office. The authors gratefully acknowledge the contributions to this work by Dr. Thomas Pulliam of NASA Ames Research Center, Moffett Field, CA and Dr. Venke Sankaran of the US Army, Aeroflightdynamics directorate, Moffett Field, CA.

References

- ¹Wissink, A. M., Sitaraman, J., Sankaran, V., Pulliam, T., and Mavriplis, D., “A Multi-Code Python-Based Infrastructure for Overset CFD with Adaptive Cartesian Grids,” AIAA Paper, 46th AIAA Aerosciences Conference, Vol. 927, Jan. 2008.
- ²Sitaraman, J., Katz, A., Jayaraman, B., Wissink, A. M., and Sankaran, V., “Evaluation of a Multi-Solver Paradigm for CFD using Unstructured and Structured Adaptive Cartesian Grids,” 46th AIAA Aerosciences Conference, Jan. 2008, AIAA Paper 2008-660.
- ³Berger, M. and Oliger, J., “Adaptive mesh refinement for hyperbolic partial differential equations,” J. Comp. Physics, Vol. 53, 1984.
- ⁴Berger, M. J. and Colella, P., “Local adaptive mesh refinement for shock hydrodynamics,” Journal of Computational Physics, Vol. 82, May 1989, pp. 64–84.
- ⁵Berger, M. and Jameson, A., “Automatic Adaptive Grid Refinement for the Euler Equations,” AIAA, Vol. 23, No. 4, Apr. 1985, pp. 561–568, MAE Report No. 1633, October 1983, Princeton University, and NYU Report No. DOE/ER/03077-202, October 1983.
- ⁶Nemec, M., Aftosmis, M. J., and Wintzer, M., “Adjoint-Based Adaptive Mesh Refinement for Complex Geometries,” 46th AIAA Aerosciences Conference, Jan. 2008, AIAA Paper 2008-725.
- ⁷Park, M. A., “Adjoint-Based, Three-Dimensional Error Prediction and Grid Adaptation,” 32nd AIAA Fluid Dynamics Conference, 2002, AIAA Paper 2002-3286.
- ⁸Venditti, D. A. and Darmofal, D. L., “Grid Adaptation for Functional Outputs: Application to Two-Dimensional Inviscid Flows,” J. Comput. Phys., Vol. 176, 2002, pp. 40–69.
- ⁹Lamb, H., Hydrodynamics, Dover Publications, 6th ed., 1993.
- ¹⁰Lugt, H. J., The dilemma of defining a vortex, Recent developments in theoretical and experimental fluid mechanics: Compressible and incompressible flows, 1979.
- ¹¹Chong, M. S., Perry, A. E., and Cantwell, B. J., “A general classification of three-dimensional flow fields,” Physics of Fluids, Vol. 2, May 1990, pp. 765–777.
- ¹²Hunt, J. C. R., Wray, A. A., and Moin, P., “Eddies, streams, and convergence zones in turbulent flows,” In its Studying Turbulence Using Numerical Simulation Databases, 2. Proceedings of the 1988 Summer Program p 193-208 (SEE N89-24538 18-34), Dec. 1988, pp. 193–208.
- ¹³Jeong, J. and Hussain, F., “On the identification of a vortex,” Journal of Fluid Mechanics, Vol. 285, 1995, pp. 69–94.

¹⁴Horiuti, K. and Takagi, Y., "Identification method for vortex sheet structures in turbulent flows," Physics of Fluids, Vol. 17, No. 12, Dec. 2005.

¹⁵Pulliam, T. H., "Solution Methods in Computational Fluid Dynamics," von Karman Institute for Fluid Mechanics Lecture Series, Numerical Techniques for Viscous Flow Computations in Turbomachinery, Jan. 1986, http://people.nas.nasa.gov/pulliam/mypapers/vki_notes/vki_notes.html.

¹⁶Hornung, R. D., Wissink, A. M., and Kohn, S. R., "Managing complex data and geometry in parallel structured AMR applications," Eng. with Comput., Vol. 22, No. 3, 2006, pp. 181–195.

¹⁷Hornung, R. D. and Kohn, S. R., "Managing application complexity in the SAMRAI object-oriented framework," Concurrency and Computation: Practice and Experience, Vol. 14, No. 5, 2002, pp. 347–368.

¹⁸Wissink, A. M., Hornung, R. D., Kohn, S. R., S., S. S., and Elliott, N., "Large scale parallel structured AMR calculations using the SAMRAI framework," Supercomputing '01: Proceedings of the 2001 ACM/IEEE conference on Supercomputing (CDROM), 2001.

¹⁹Truesdell, C., The kinematics of vorticity, Indiana University Press, 1954.

²⁰Horiuti, K., "A classification method for vortex sheet and tube structures in turbulent flows," Physics of Fluids, Vol. 13, Dec. 2001, pp. 3756–3774.

²¹Horiuti, K., "Roles of non-aligned eigenvectors of strain-rate and subgrid-scale stress tensors in turbulence generation," Journal of Fluid Mechanics, Vol. 491, Sep. 2003, pp. 65–100.

²²Sitaraman, J. and Baeder, J. D., "Evaluation of the Wake Prediction Methodologies used in CFD Based Rotor Airload Computations," 24th Applied Aerodynamics Conference, Jun. 2006, AIAA Paper 2006-3472.

²³Sitaraman, J., Floros, M., Wissink, A. M., and Potsdam, M., "Parallel Unsteady Overset Mesh Methodology for a Multi-Solver Paradigm with Adaptive Cartesian Grids," 26th Applied Aerodynamics Conference, Jan. 2008, AIAA Paper 2008-7117.